# About the Transferability of Topographic Correction Methods From Spaceborne to Airborne Optical Data

Marius Vögtli, Daniel Schläpfer, *Member, IEEE*, Rudolf Richter, Andreas Hueni, *Member, IEEE*, Michael E. Schaepman, *Senior Member, IEEE*, and Mathias Kneubühler

***Abstract*—In rugged terrain, topography substantially influences the illumination and observation geometry, and thus, the bidirectional reflectance distribution function (BRDF) of a surface. While this problem has been known and investigated for spaceborne optical data since the 1980s, it has led to several well-known topographic correction methods. To date, the methods developed for spaceborne data were equivalently applied to airborne data with distinctly higher spatial resolution, illumination/observation angle configurations and finally (instantaneous) field of view (FOV). On the one hand, this article evaluates, whether such a transfer of methods from spaceborne to airborne acquisitions is reasonable. On the other hand, a new Lambertian/statistical-empirical correction method is introduced. While in the spaceborne case the Modified Minnaert (MM) and the Statistical-Empirical (SE) methods performed best, MM led to the statistically and visually best compromise for the airborne data. Our results suggest further that with a higher spatial resolution various effects come into play (FOV widening; changing the fraction of geometric, volumetric and isotropic scattering, etc.), compromising previously successful methods, such as the SE method.**

***Index Terms*—Airborne, rugged terrain, spaceborne, topographic correction.**

## I. Introduction

THE measurement of the electromagnetic radiation of every surface is subject to the illumination geometry and the observation geometry and described by the surface's bidirectional reflectance distribution function (BRDF, [1]). In rugged, mountainous terrain, topography has a strong influence on the illumination geometry. The variability in terrain slope and aspect and, thus, in orientation toward the sun leads to changes in brightness for the same surface cover, which for instance increases the uncertainty of value-added products [2]. The objective of topographic correction is to compensate for the illumination conditions and to provide an image as if recorded for a corresponding flat terrain. However, since the scene also depends on target-specific BRDF effects, this requires the per-pixel BRDF knowledge as well, which is difficult to obtain for high spatial resolution satellite and airborne scenes. The influence of topographic effects on the incidence geometry of optical satellite imagery has been widely investigated since the 1980s [3]–[7]. Models for the combined atmospheric/topographic compensation based on radiative transfer codes followed in the 1990s [8]–[11]. Nowadays, several established methods for the correction of incidence geometry effects (often referred to as *topographic correction methods*) are readily available, such as the *cosine method*, the *Minnaert method*, the *C-correction method*, or the *Statistical-Empirical method* (see Section III-B).

Sola *et al.* [12] employed a multicriteria evaluation of ten widely used topographic correction methods, applied to SPOT-5 scenes in the Pyrenee mountains. The best ranking was obtained for the SE method. In an earlier study using Landsat imagery, Hantson and Chuvieco[13] came to a similar conclusion. Recently, Ma *et al.* [14] analyzed the uncertainty propagation chain of two semiempirical topographic correction models. A simplified terrain/BRDF model restricted to vegetation canopies was published for Landsat-8 OLI data [15]. Even the simplified 1-D model is complex, requiring input data about the canopy structure and optical parameters, which is difficult to get on a global scale. In addition, a homogeneous canopy cover per scene is assumed. Also, the influence of the surrounding terrain is neglected. Therefore, this article concentrates on general purpose topographic correction models suitable for the operational processing of large data volumes.

As opposed to optical spaceborne data, no specific topographic correction methods have been published for optical airborne imagery so far. In most cases, the well-known algorithms developed for optical satellite imagery are adopted. This can be problematic for several reasons, as follows.

i) In most cases, optical airborne sensors have a distinctly higher spatial resolution than their spaceborne counterparts. On the one hand, a higher spatial resolution can lead to a larger amount of BRDF effects present in data acquisitions, on the other hand to a generally higher variation in image statistics. Moreover, the smaller coverage may lead to statistically nonrepresentative sampling with respect to the variability of surface cover types and the distribution of terrain angles.

ii) Airborne sensors exhibit a generally higher variability in acquisition geometry. While spaceborne sensors have well-known and well-described orbits, the image acquisition of airborne sensors is subject to various factors, such as platform stability and acquisition time. In combination with the generally

Manuscript received August 1, 2020; revised October 29, 2020; accepted November 14, 2020. Date of publication November 19, 2020; date of current version January 6, 2021. *(Corresponding author: Marius Vögtli.)*

Marius Vögtli, Andreas Hueni, Michael E. Schaepman, and Mathias Kneubühler are with the University of Zurich, CH-8057 Zurich, Switzerland (e-mail: marius.voegtli@geo.uzh.ch; ahueni@geo.uzh.ch; michael.schaepman@geo.uzh.ch; kneub@geo.uzh.ch).

Daniel Schläpfer is with ReSe Applications LLC, CH-9500 Wil, Switzerland (e-mail: daniel@rese.ch).

Rudolf Richter is with German Aerospace Center (DLR), D-82234 Wessling, Germany (e-mail: rudolf.richter@dlr.de).

Digital Object Identifier 10.1109/JSTARS.2020.3039327

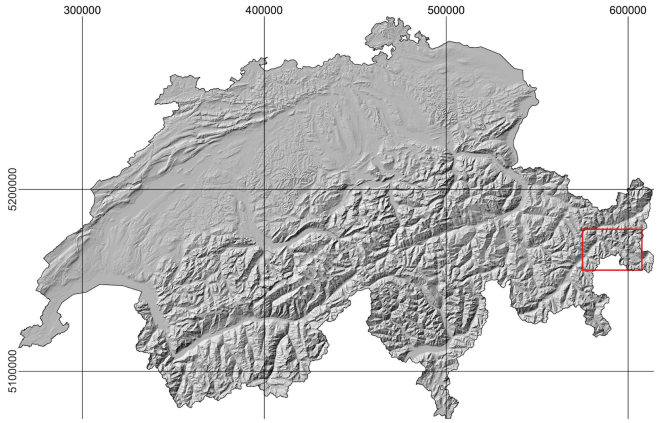


Fig. 1. Location of the study site within Switzerland. Coordinates: UTM 32N. Background: swisstopo *DHM25*, displayed as hillshade.

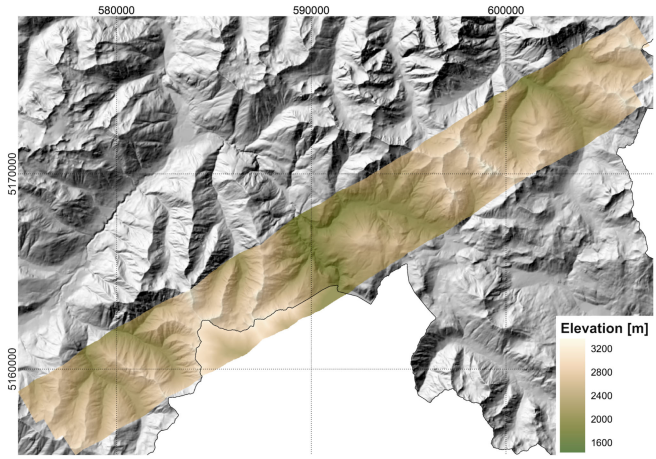


Fig. 2. Elevation of the study site. Coordinates: UTM 32N. Background: swisstopo *DHM25*, displayed as hillshade. Elevation colormap: *oleron* from [16].

larger field of view (FOV) than spaceborne sensors, this leads to a wider range of combinations of slope, aspect, solar angles, and pixel viewing angles to be considered.

Consequently, this article evaluates differences of topographic correction methods for both spaceborne and airborne images of a Swiss Alpine landscape, exhibiting a rugged terrain. Using Sentinel-2 spaceborne multispectral data and APEX airborne imaging spectroscopy data, the influence of the spatial resolution and extent on the correction of topography effects, and thus, the transferability of methods originally developed for spaceborne instruments to the airborne data acquisition situation is investigated.

Our observations with existing methods have shown that statistical-empirical approaches show advantages in steep terrain whereas the purely physical Lambertian approach leads to stable corrections with moderate slopes. Therefore, we also investigate a new operational merged physical-empirical approach to topographic correction, taking advantage of a physical part to evaluate surface reflectance and a semiempirical part to minimize inherent problems of the physical approach in faintly illuminated areas.

This article is organised as follows. Section II presents the spaceborne and airborne datasets and their preprocessing. Section III describes the established topographic correction methods and introduces our new merged physical-empirical approach. Section IV provides detailed results (statistical, visual) for the spaceborne and airborne scenes obtained from a processing with the established and new topographic correction methods. Section V discusses the results and conclusions are given in Section VI.

## II. Material

### A. Study Site

The study site is situated in a mountainous landscape in the south-eastern part of Switzerland and slightly touching Italy and Austria (see Fig. 1). As can be seen in Fig. 2, elevations range from roughly 1600 to 3200 m. The terrain is characterized by an average slope of around 30° (ranging from 0° to 80°) and two main aspects of around 50° (approximately NE) and 230° (approximately SW). Vegetation consisting of forests, meadows, and alpine shrublands makes up approximately 50% of the land cover, while the rest is shaped by bare soil, rocks, water bodies, and patches of perennial snow.

TABLE I
Overview of the 13 Bands of Sentinel-2 A

| Band | Wavelength [nm] | Resolution [m] |
|---|---|---|
| 1 | 442.7 | 60 |
| 2 | 492.4 | 10 |
| 3 | 559.8 | 10 |
| 4 | 664.6 | 10 |
| 5 | 704.1 | 20 |
| 6 | 740.5 | 20 |
| 7 | 782.8 | 20 |
| 8 | 832.8 | 10 |
| 8A | 864.7 | 20 |
| 9 | 945.1 | 60 |
| 10 | 1373.5 | 60 |
| 11 | 1613.7 | 20 |
| 12 | 2202.4 | 20 |

See [17] for further information on Sentinel-2.

### B. Sentinel-2 Image Data

For the spaceborne case, we used a Level-1C Sentinel-2A scene from July 16, 2019 (10:20 UTC) with a mean solar zenith angle (SZA) of 27.8° and a mean solar azimuth angle (SAA) of 149.4°. Sentinel-2 acquires data in 13 spectral bands from 440 to 2200 nm with spatial resolutions of 10, 20, and 60 m (see Table I) [17]. The swath of a full scene covers an area of 290 × 290 km. Using ATCOR-3 [18], the image data were converted to top-of-atmosphere (TOA) radiance. In order to work with only one spatial resolution, the bands with a spatial resolution of 10 m or 60 m were resampled to fit the majority of bands, i.e., to a resolution of 20 m.

TABLE II
UTC ACQUISITION TIME (AT), SOLAR ZENITH ANGLE (SZA), SOLAR AZIMUTH ANGLE (SAA), AND HEADING OF THE FLIGHT LINES (FLN) USED FOR THIS STUDY

| | AT [UTC] | SZA [°] | SAA [°] | Heading [°] |
|---|---|---|---|---|
| **FLn A** | 0914 - 0923 | 36.1 | 123.6 | 59.4 |
| **FLn B** | 0926 - 0935 | 34.4 | 127.4 | 242.0 |
| **FLn C** | 0938 - 0947 | 32.8 | 131.6 | 59.4 |

### C. APEX Image Data

The three airborne flight lines (FLn) were acquired on July 16, 2019 by the Airborne Prism EXperiment (APEX) imaging spectrometer [19], mounted on a Cessna 208 Grand Caravan aircraft. Table II summarises several key characteristics of the three flight lines. APEX was flown at an altitude of around 6400 m above mean sea level and approximately 5000 m above ground, yielding a ground sample distance of 2 m. The APEX data were orthorectified to a geometric accuracy of 1 to 2 pixels using the PARGE image rectification software [20].

The radiometric processing from raw data to at-sensor radiance was carried out in the APEX processing and archiving facility [21] using radiometric gains and offsets obtained from laboratory measurements in spring 2019. After radiometric processing, APEX covers a wavelength range of 376 to 2508 nm with 299 bands. Using ATCOR-4's [18] TOARAD module, the APEX image data were spectrally resampled to the 13 Sentinel-2 bands (see Table I).

### D. Elevation Data

Two different digital elevation models (DEMs) from the Swiss Federal Office of Topography (swisstopo) were used for the processing. For the Sentinel-2 data, the *DHM25* product with a pixel size of 25 m and a vertical accuracy of 1.5 to 8 m was used. The DEM was resampled to a horizontal resolution of 20 m using a bilinear interpolation. For the spatially higher resolved APEX data, the *swissALTI3D* product with a pixel size of 2 m and a vertical accuracy of 0.5 to 3 m was applied.

## III. METHODS

### A. Atmospheric and Topographic Correction

The preprocessed Sentinel-2 and APEX radiance data were atmospherically and topographically processed to ground reflectance data [bottom of atmosphere (BOA) reflectance] using the rugged terrain modules of ATCOR-3/4 [18]. The flowchart in Fig. 3 provides an overview of the general processing chain. Employing the MODTRAN 5 [22] code, a database of atmospheric look-up tables for a wide range of atmospheric parameters, solar and observation geometries, and ground elevations is calculated. The atmospheric compensation includes the retrieval of atmospheric parameters (aerosol optical thickness at 550 nm, water vapor column) using a radiative transfer model. For both sensors, the water vapor correction was performed using the 940 nm region. For this purpose, the atmospheric precorrected differential absorption algorithm is used [23]. The method can achieve a relative water vapor retrieval accuracy of about 5% for imaging spectroscopy data, and about 10% if only two retrieval bands are available (Sentinel-2 bands at 865 nm and 945 nm) [24]. For the topographic correction component of the atmospheric compensation, the various methods described in the following Sections III-B and III-C were applied.

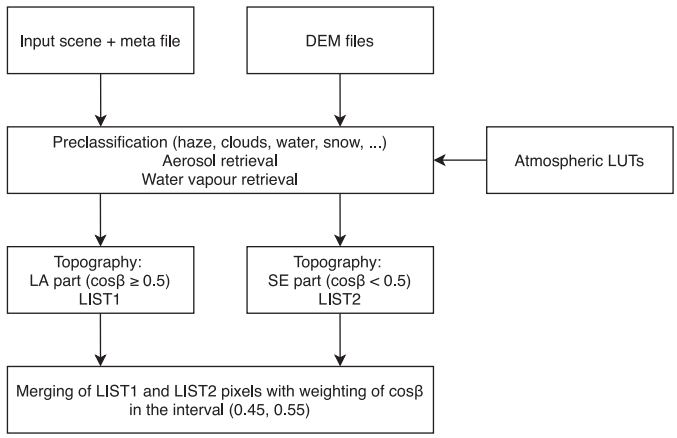


Fig. 3. Flowchart of the data processing, detailing the new LA+SE method.

### B. Established Topographic Correction Methods

This section summarises known topographic correction methods. The methods are implemented in the ATCOR code family. Therefore, the terminology in this article is used based on the description in the ATCOR documentation; more details about their implementation can be found in [18]. Due to their empirical character, all methods may either be applied to TOA radiance, TOA reflectance, or BOA reflectance. With this in mind, a generic quantity $g_t$ is used for a pixel value in rugged terrain and the value $g_h$ is the corresponding value for a horizontal plane.

Following [25], topographic processing methods can be grouped into Lambertian and non-Lambertian, depending on the TOA radiance/reflectance being treated as independent of observer and solar geometry or not. They require a DEM to obtain the per-pixel slope and aspect (azimuth) angles needed to calculate the local SZA $\beta$

$$\cos\beta = \cos\theta_s \cos\theta_p + \sin\theta_s \sin\theta_p \cos(\phi_s - \phi_p) \quad (1)$$

where $\theta_s$, $\theta_p$, $\phi_s$, $\phi_p$ are the solar zenith, pixel slope, solar azimuth, pixel azimuth angles, respectively. $\cos\beta$ is required for all topographic compensation algorithms.

*1) Cosine Method (LA):* The standard Lambertian topographic correction method is the "cosine method," proposed by [6]. The corrected value is calculated as

$$g_h = g_t \frac{\cos\theta_s}{\cos\beta}. \quad (2)$$

This equation shows a principal limitation: as the local zenith angle $\beta$ tends to 90°, $\cos\beta$ tends to zero, and $g_h$ to infinity.

*2) Minnaert Method (M):* The Minnaert approach [26] and its variants have been designed to treat the problem of the Lambertian assumption of a perfectly diffuse reflector, because most

natural surfaces show bidirectional reflectance properties [27]–[30]. It uses a wavelength-dependent constant $k_i$ to improve the correction for channel $i$

$$g_h(i) = g_t(i)\left(\frac{\cos\theta_s}{\cos\beta}\right)^{k_i}. \tag{3}$$

Equations (2) and (3) are based on the assumption of a single, directional illumination source from the direction $\theta_s$, $\phi_s$ on the surface. Illumination by diffuse solar flux from all directions is neglected.

*3) Modified Minnaert (MM) Method:* An empirical modification of the Minnaert approach, named "Modified Minnaert," was presented in [2]. The method uses a set of empirical rules with a modified illumination angle $\beta_T$

$$g_h(i) = g_t(i)\left(\frac{\cos\theta_s}{\cos\beta_T}\right)^{b_i}. \tag{4}$$

The angle $\beta_T$ is given by the sum of SZA and an empirical threshold angle of the scene. The exponent $b$ depends on wavelength and vegetation cover (see [2] for details).

*4) C-correction (CC) Method:* The CC method was introduced by [6] as a semiempirical non-Lambertian algorithm to account for the diffuse solar illumination and using image statistics for the correction

$$g_h(i) = g_t(i)\frac{\cos\theta_s + c_i}{\cos\beta + c_i} \tag{5}$$

where $i$ is the channel index, $c_i = \frac{b_i}{m_i}$, and $b_i$ and $m_i$ are offset and slope, respectively, obtained from a linear regression of $g_t$ versus $\cos\beta$.

*5) Statistical-Empirical (SE) Method:* The SE method was also proposed by Teillet [6] to reduce topographic effects based on the average difference between scene brightness and exposition-dependent illumination changes. It can be formulated as

$$g_h(i) = g_t(i) - m_i\cos\beta - b_i + \bar{g}_t(i) \tag{6}$$

where $\bar{g}_t(i)$ is the scene-average TOA radiance or reflectance. A variant of this equation is

$$g_h(i) = g_t(i) + m_i(\cos\theta_s - \cos\beta) \tag{7}$$

where the topography correction depends only on the difference $\cos\theta_s - \cos\beta$ weighted with the slope $m_i$ of the regression equation. Visually, the image results of (6) and (7) cannot be distinguished, and the statistics are similar. But the SE variant sometimes yields better spectral results; therefore, the latter is used in our analysis.

We excluded snow and cloud pixels from the SE method's image statistics. The inclusion of snowy areas will deteriorate the quality of topographic correction for the nonsnow pixels as the BRDF of snow is distinctly different from the other surface covers [31], [32].

### C. Merged Topographic Correction Method

In addition to the abovementioned methods, we propose a new variation, called "LA+SE," merging a physical topographic correction (Lambertian, LA) with an empirical one (Statistical-Empirical, SE). The reason is that the illposed nature of inverse problems in remote sensing counteracts a fully physics-based approach to topographic correction, specifically in steep terrain where the illumination field and the target-specific incidence BRDF variations are not well known. The physical part calculates the BOA reflectance in rugged terrain with some simplifying assumptions. It uses the ATCOR atmospheric compensation methods [18]. Our method consists of a merging of two parts, which are now presented.

*Algorithm 1: Lambertian Cosine Correction:* This part describes the retrieval of surface reflectance in rugged terrain and its simplifying assumptions. The measured TOA radiance consists of the following four components:

1) path radiance $L_p$, representing the radiance scattered by the atmosphere into the detector FOV;
2) ground reflected target pixel radiance $L_g$;
3) adjacency radiance $L_a$, i.e., radiance reflected by neighboring surfaces outside the detector FOV but scattered by the atmosphere into the detector FOV; and
4) terrain radiance from adjacent slopes $L_t$ reflected by the ground target pixel.

$$L_{\text{TOA}} = L_p + L_g + L_a + L_t. \tag{8}$$

The dependencies from position ($x$, $y$, $z$), wavelength $\lambda$, solar and sensor view geometry, and atmospheric parameters are omitted in the notation for brevity. The terrain radiance component is then

$$L_t = T\,E_t^{(1)}\,V_t\,\rho_t/\pi \tag{9}$$

where $T$ is the total (direct plus diffuse) ground-to-sensor transmittance, $E_t^{(1)}$ the global terrain flux, and $V_t$ the terrain-view factor. The unknown $\rho_t$ is initialized with 0.1, but will be iterated. To handle the difficult terrain influence, the terrain-view factor $V_t$ has to be computed, which represents a map of all pixels that can contribute to the reflected terrain radiation on an individual pixel. It is the complement of the sky-view factor $V_s$, i.e., $V_t = 1 - V_s$ (if $V_s$ for the hemisphere is normalized to 1), and $V_s$ can be computed with the fast ray tracing of the Dozier algorithm [33].

The BOA reflectance $\rho$ corresponding to $L_g$ is calculated depending on the direct and diffuse pixel irradiance, neglecting the neighborhood influence

$$\rho = \frac{\pi\,[L_{\text{TOA}} - L_p]}{T\,[b\,E_s\cos\beta + E_d^*]} \tag{10}$$

where $b = 0$ for a shadow pixel, else $b = 1$, $E_s$ is the direct solar beam irradiance (at ground), and $E_d^*$ is the total diffuse flux on a sloped surface [34]. Unlike the TOA radiance/reflectance equations [see (2) and (3)] for the cosine and Minnaert cases, the ground reflectance of this equation does not tend to infinity as $\cos\beta$ tends to zero, because the diffuse flux $E_d^*$ is always greater than zero. So this is an advantage, but does not imply that the results are always physically correct, because of the difficulty of calculating the diffuse and terrain flux in a complex environment.

Equation (10) is then iterated to include the first-order correction with the terrain influence

$$\rho^{(1)} = \frac{\pi\ [L_{\text{TOA}} - L_p]}{T\ \left[b\, E_s \cos\beta + E_d^* + E_t^{(1)}\right]}. \tag{11}$$

Next, the average reflectance $\bar{\rho}^{(1)}$ is calculated with a moving low-pass window of size $2R_1 \times 2R_1$, with the typical adjacency range $R_1 = 0.5$ to 1 km (airborne) or 1 to 2 km (spaceborne).

One more iteration on the terrain irradiance yields the BOA reflectance $\rho^{(2)}$. The adjacency effect is accounted for by computing the average reflectance $\bar{\rho}^{(2)}(x, y)$ with a moving low-pass window of size $2R_1 \times 2R_1$. Then, the final step updates the ground reflectance $\rho^{(2)}$ with the weighted difference of the area-average $\bar{\rho}^{(2)}$ and $\rho^{(2)}$ using the weight factor $q$ = ratio of diffuse to direct ground-sensor transmittance [10]

$$\rho_{p1}(x, y) = \rho^{(2)}(x, y) + q(x, y)\ \left[\rho^{(2)}(x, y) - \bar{\rho}^{(2)}(x, y)\right] \tag{12}$$

where the index "$p1$" indicates the result of the "part 1" of the algorithm.

*Algorithm 2: Statistical-Empirical Correction:* The second part of our method employs the SE topographic correction. Similar to the first part, the evaluation has to be performed for the whole scene. The SE approach (7), is applied to the surface reflectance product based on the elevation information from the DEM, but uses flat (horizontal) surface elements, i.e., omitting the $x$, $y$ planar coordinates

$$\rho^{(3)}(\lambda, z) = \frac{\pi\ [L_{\text{TOA}}(\lambda, z) - L_p(\lambda, z)]}{T(\lambda, z)\ [E_s(\lambda, z) + E_d(\lambda, z)]} \tag{13}$$

where $E_d$ is the downwelling diffuse solar flux on a horizontal plane, i.e., the counterpart of $E_d^*$ for an inclined plane. This means, the terrain slope and terrain reflected radiance $L_t$ is not explicitly taken into account, but the effects are implicitly included in the statistical regression of the (assumed flat) surface elements with the $\cos\beta$, i.e., the parameter $m_i$ of (6) is calculated for each channel. Then, the term $g_t$ of (6) is $\rho$ of (13), and the terrain corrected surface reflectance value is

$$\rho_{\text{SE},i} = \rho_i^{(3)} + m_i\,(\cos\theta_s - \cos\beta). \tag{14}$$

Omitting the channel index for brevity, the last step is the adjacency correction (with index "$p2$" for algorithm "part 2"), which is conducted as for the part 1 algorithm (12)

$$\rho_{p2}(x, y) = \rho_{\text{SE}}(x, y) + q(x, y)\ \left[\rho_{\text{SE}}(x, y) - \bar{\rho}_{\text{SE}}(x, y)\right]. \tag{15}$$

We also tested a version, where the multiple terrain reflected radiation effects from nearby opposite slopes are included before running the SE compensation, but degraded results were obtained, i.e., it is better to let the SE algorithm handle these effects.

*3) Merging Phase:* This phase merges the products $\rho_{p1}(x, y)$ and $\rho_{p2}(x, y)$ as follows: let LIST1 be the list of pixels with $\cos\beta \geq 0.5$ and LIST2 the list with $\cos\beta < 0.5$. Then, the final product merges the LIST1 pixels from algorithm 1 with the LIST2 pixels of algorithm 2

$$\begin{aligned}\rho_i(\text{LIST1}) &= \rho_{p1,i}(\text{LIST1})\\ \rho_i(\text{LIST2}) &= \rho_{p2,i}(\text{LIST2}).\end{aligned} \tag{16}$$

An analysis of different thresholds showed that 0.5 usually performs best. In some cases, slight variations might further improve the result. Occasionally, the threshold $\cos\beta \geq T_\beta = 0.5$ causes brightness steps in areas around this threshold. Therefore, the last step of the merging calculates the LIST3 of pixels with $\cos\beta$ in the interval (0.45, 0.55) and weights the values of the LIST1, LIST2 pixels, which are found in LIST3 by a linear transition between the following two methods:

$$\begin{aligned}\rho_i(\text{LIST3}) = {}& \rho_i(\text{LIST3}(\text{LIST1}))(0.55 - \cos\beta)/0.1\\ &+ \rho_i(\text{LIST3}(\text{LIST2}))(\cos\beta - 0.45)/0.1.\end{aligned} \tag{17}$$

This removes visual brightness steps in the LA+SE product for all practical purposes.

### D. Evaluation

For the evaluation, cloud and water pixels as well as cast shadows were excluded from the two datasets. In order to analyze the same land cover, the Sentinel-2 scene was cut to the outline of the three APEX flight lines. All analyses were calculated on the whole study site and on a vegetation and a bare soil land cover subset. The two subsets were built using spectral indices.

Different quantitative methods were applied to evaluate the quality of each topographic correction method. After a successful correction, the measured reflectance should be independent of the local illumination condition $\cos\beta$. This was assessed using the following two statistical measures: the $R^2$ value and the slope of a linear regression between reflectance and illumination condition. Since for each band the value of the slope depends on the magnitude of the reflectance factor, the slope of the linear regression was normalized by the mean reflectance per band to compensate these wavelength-dependent brightness differences.

## IV. Results

### A. Sentinel-2

Table III shows the absolute values of the wavelength-normalized slope of a linear fit between Sentinel-2 reflectance data and the illumination condition $\cos\beta$ for 13 wavelengths and six different correction methods, analyzed over the whole study site (i.e., all land cover types). Overall, the Modified Minnaert (MM) method scored best with a mean value of 0.237, followed by the C-correction (CC) method with a value of 0.268, the Statistical-Empirical (SE) method with a value of 0.296, the merged Lambertian/Statistical-Empirical (LA+SE) method with a value of 0.305, no topographic correction (NC) with a value of 0.733, and a pure Lambertian cosine correction (LA) with a value of 0.735. There was a strong wavelength dependence of the results. In the visible wavelengths up to 704.1 nm, SE showed the lowest values, while MM had considerably high values. Starting

TABLE III
WAVELENGTH-NORMALIZED SLOPE OF A LINEAR FIT BETWEEN REFLECTANCE AND ILLUMINATION CONDITION FOR 13 SENTINEL-2 BANDS

| | Wavelength [nm] | | | | | | | | | | | | | |
|---|---|---|---|---|---|---|---|---|---|---|---|---|---|---|
| | **442.7** | **492.4** | **559.8** | **664.6** | **704.1** | **740.5** | **782.8** | **832.8** | **864.7** | **945.1** | **1373.5** | **1613.7** | **2202.4** | **Mean** |
| **NC** | 0.419 | 0.559 | 0.595 | 0.601 | 0.702 | 0.807 | 0.824 | 0.840 | 0.849 | 0.804 | 0.848 | 0.877 | 0.806 | 0.733 |
| **LA** | 1.238 | 1.092 | 0.994 | 1.029 | 0.829 | 0.572 | 0.529 | 0.501 | 0.482 | 0.490 | 0.522 | 0.544 | 0.727 | 0.735 |
| **MM** | 0.623 | 0.483 | 0.395 | 0.423 | 0.245 | **0.146** | **0.114** | **0.090** | **0.073** | **0.084** | **0.088** | **0.092** | 0.225 | **0.237** |
| **CC** | 0.271 | 0.335 | 0.365 | 0.360 | 0.326 | 0.242 | 0.229 | 0.229 | 0.207 | 0.211 | 0.223 | 0.231 | 0.253 | 0.268 |
| **SE** | **0.026** | **0.043** | **0.152** | **0.038** | **0.192** | 0.505 | 0.573 | 0.577 | 0.563 | 0.551 | 0.353 | 0.214 | **0.057** | 0.296 |
| **LA+SE** | 0.412 | 0.346 | 0.352 | 0.311 | 0.300 | 0.330 | 0.339 | 0.329 | 0.316 | 0.321 | 0.241 | 0.184 | 0.182 | 0.305 |

Lowest values per wavelength are highlighted with bold letters.

TABLE IV
$R^2$ OF A LINEAR REGRESSION BETWEEN REFLECTANCE AND ILLUMINATION CONDITION FOR 13 SENTINEL-2 BANDS

| | Wavelength [nm] | | | | | | | | | | | | | |
|---|---|---|---|---|---|---|---|---|---|---|---|---|---|---|
| | **442.7** | **492.4** | **559.8** | **664.6** | **704.1** | **740.5** | **782.8** | **832.8** | **864.7** | **945.1** | **1373.5** | **1613.7** | **2202.4** | **Mean** |
| **NC** | 0.006 | 0.012 | 0.024 | 0.020 | 0.063 | 0.161 | 0.163 | 0.162 | 0.170 | 0.175 | 0.202 | 0.163 | 0.100 | 0.109 |
| **LA** | 0.067 | 0.054 | 0.071 | 0.061 | 0.088 | 0.090 | 0.076 | 0.066 | 0.063 | 0.075 | 0.086 | 0.068 | 0.079 | 0.073 |
| **MM** | 0.018 | 0.011 | 0.012 | 0.011 | 0.008 | **0.006** | **0.004** | **0.002** | **0.001** | **0.002** | **0.003** | **0.002** | 0.009 | **0.007** |
| **CC** | 0.004 | 0.006 | 0.011 | 0.008 | 0.015 | 0.018 | 0.015 | 0.015 | 0.012 | 0.015 | 0.017 | 0.013 | 0.011 | 0.012 |
| **SE** | **0.000** | **0.000** | **0.002** | **0.000** | **0.005** | 0.075 | 0.091 | 0.088 | 0.087 | 0.094 | 0.043 | 0.012 | **0.001** | 0.038 |
| **LA+SE** | 0.008 | 0.006 | 0.010 | 0.006 | 0.013 | 0.034 | 0.035 | 0.032 | 0.030 | 0.036 | 0.021 | 0.009 | 0.006 | 0.019 |

Lowest values per wavelength are highlighted with bold letters.

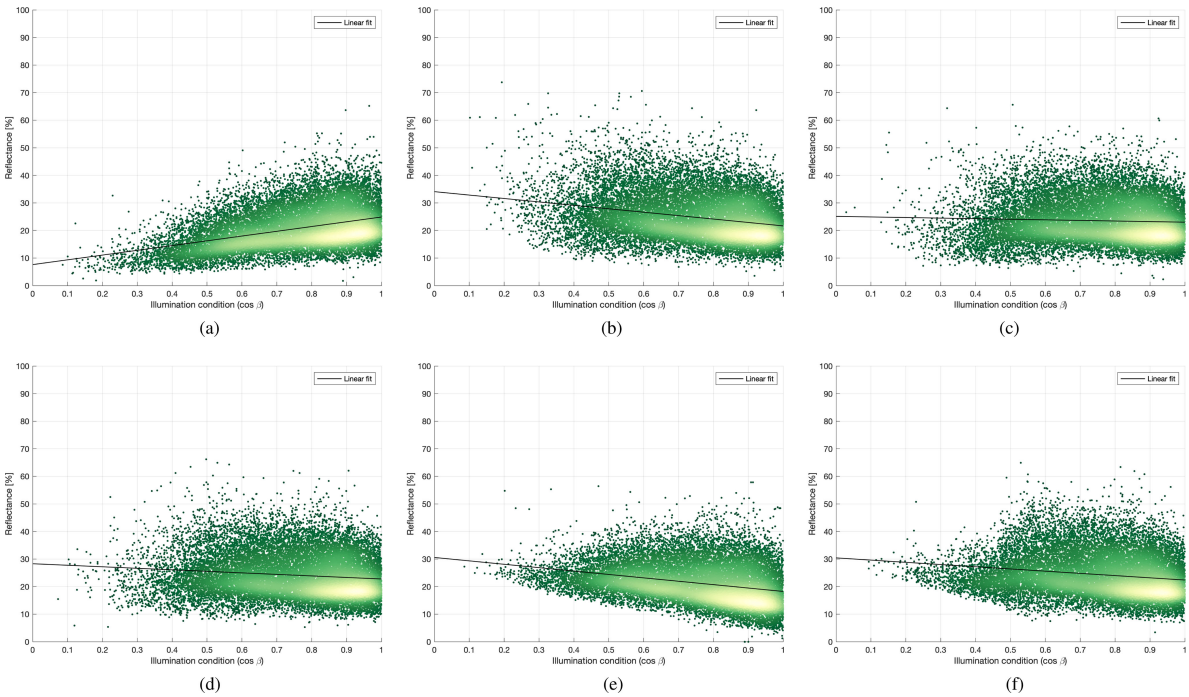


Fig. 4. Relation between reflectance in band 8 (832.8 nm) and illumination condition ($\cos\beta$) of the Sentinel-2 scene for different topographic correction methods. (a) No correction (NC). (b) Lambertian cosine correction (LA). (c) Modified Minnaert (MM). (d) C-correction (CC). (e) Statistical-Empirical (SE). (f) Merged LA+SE.

at 740.5 nm, this behavior turned to the opposite. There, MM had distinctly lower values than SE. $R^2$ values of a linear regression between reflectance and illumination showed a similar pattern (see Table IV). Here too, MM had the lowest mean value of 0.007, followed by CC (0.012), LA+SE (0.019), SE (0.038), LA (0.073), and NC (0.109). The same wavelength-dependent behavior of MM and SE appeared. The impact of the different correction methods on the relation between the reflectance and the illumination condition, shown for the whole scene and at an exemplary wavelength of 832.8 nm can be observed in Fig. 4.

Analyses for the vegetation and bare soil subsets showed a similar picture (see Tables VIII to XI in the Appendix). With some exceptions, mainly in the lower wavelengths, MM led to the lowest values for the majority of wavelengths with a

TABLE V
WAVELENGTH-NORMALIZED SLOPE OF A LINEAR FIT BETWEEN REFLECTANCE AND ILLUMINATION CONDITION FOR 13 APEX BANDS, AVERAGED OVER THREE FLIGHT LINES

| | Wavelength [nm] | | | | | | | | | | | | | |
|---|---|---|---|---|---|---|---|---|---|---|---|---|---|---|
| | **442.7** | **492.4** | **559.8** | **664.6** | **704.1** | **740.5** | **782.8** | **832.8** | **864.7** | **945.1** | **1373.5** | **1613.7** | **2202.4** | **Mean** |
| **NC** | 0.714 | 0.686 | 0.717 | 0.756 | 0.826 | 0.891 | 0.913 | 0.929 | 0.939 | 0.973 | 0.994 | 1.012 | 0.923 | 0.867 |
| **LA** | 0.984 | 0.954 | 0.855 | 0.824 | 0.678 | 0.480 | 0.426 | 0.398 | 0.373 | 0.375 | 0.418 | 0.452 | 0.680 | 0.608 |
| **MM** | 0.223 | **0.185** | **0.166** | 0.183 | 0.210 | 0.151 | 0.192 | 0.216 | 0.237 | 0.244 | 0.237 | 0.232 | 0.070 | 0.196 |
| **CC** | 0.328 | 0.312 | 0.304 | 0.327 | 0.282 | 0.215 | 0.203 | 0.198 | 0.196 | 0.186 | 0.218 | 0.243 | 0.274 | 0.253 |
| **SE** | 0.242 | 0.235 | 0.224 | 0.227 | 0.190 | 0.145 | 0.136 | 0.130 | 0.127 | 0.119 | 0.121 | 0.123 | 0.154 | 0.167 |
| **LA+SE** | **0.195** | 0.202 | 0.184 | **0.179** | **0.126** | **0.079** | **0.068** | **0.060** | **0.062** | **0.053** | **0.024** | **0.009** | **0.055** | **0.100** |

Lowest values per wavelength are highlighted with bold letters.

TABLE VI
$R^2$ OF A LINEAR REGRESSION BETWEEN REFLECTANCE AND ILLUMINATION CONDITION FOR 13 APEX BANDS, AVERAGED OVER THREE FLIGHT LINES

| | Wavelength [nm] | | | | | | | | | | | | | |
|---|---|---|---|---|---|---|---|---|---|---|---|---|---|---|
| | **442.7** | **492.4** | **559.8** | **664.6** | **704.1** | **740.5** | **782.8** | **832.8** | **864.7** | **945.1** | **1373.5** | **1613.7** | **2202.4** | **Mean** |
| **NC** | 0.031 | 0.039 | 0.065 | 0.056 | 0.133 | 0.210 | 0.202 | 0.205 | 0.207 | 0.219 | 0.267 | 0.219 | 0.144 | 0.154 |
| **LA** | 0.067 | 0.079 | 0.095 | 0.069 | 0.098 | 0.074 | 0.056 | 0.049 | 0.044 | 0.049 | 0.065 | 0.053 | 0.082 | 0.068 |
| **MM** | 0.005 | **0.004** | **0.004** | **0.003** | 0.012 | 0.009 | 0.013 | 0.015 | 0.018 | 0.020 | 0.022 | 0.016 | 0.001 | 0.011 |
| **CC** | 0.007 | 0.009 | 0.012 | 0.011 | 0.018 | 0.017 | 0.015 | 0.014 | 0.014 | 0.013 | 0.019 | 0.017 | 0.014 | 0.014 |
| **SE** | **0.004** | 0.005 | 0.006 | 0.005 | 0.008 | 0.008 | 0.007 | 0.007 | 0.007 | 0.006 | 0.007 | 0.005 | 0.005 | 0.006 |
| **LA+SE** | 0.005 | 0.006 | 0.007 | 0.005 | **0.005** | **0.003** | **0.002** | **0.002** | **0.002** | **0.001** | **0.000** | **0.000** | **0.001** | **0.003** |

Lowest values per wavelength are highlighted with bold letters.

mean slope ($R^2$) value of 0.259 (0.016) and 0.352 (0.024) for vegetation and bare soil, respectively, followed by CC with a slope ($R^2$) of 0.267 (0.018) for vegetation and 0.378 (0.031) for bare soil.

### B. APEX

The absolute values of the wavelength-normalized slope of a linear fit between APEX BOA reflectance data and the illumination condition ($\cos\beta$) for 13 wavelengths and six different correction methods can be extracted from Table V. The values were averaged over the three APEX flight lines. With a mean value of 0.100, LA+SE showed the lowest values throughout all wavelengths, except for 492.4 nm and 559.8 nm. The second lowest mean value was obtained from the SE method (0.167), followed by the MM method (0.196), the CC method (0.253), the LA cosine correction method (0.608), and finally by NC with a value of 0.867. $R^2$ values of a linear regression between the reflectance and illumination condition show a largely similar pattern (see Table VI). Here again, LA+SE had the lowest mean value of 0.003, followed by SE (0.006), MM (0.011), CC (0.014), LA (0.068), and NC (0.154). This can further be observed in Fig. 5, showing the relation between the reflectance and the illumination condition ($\cos\beta$) of APEX flight line A for the whole scene and at an exemplary wavelength of 832.8 nm.

In the vegetation subset (Tables XII and XIII in the Appendix), MM showed the smallest mean values for both slope (0.219) and $R^2$ (0.015), while LA+SE showed the second smallest values (slope $= 0.323$, $R^2 = 0.026$). Similar to the vegetation subset, MM had the lowest mean slope in the bare soil subset (Tables VII and VIII in the Appendix) with a value of 0.157, slightly lower than LA+SE with a value of 0.158. With regard to the $R^2$, however, the two methods changed ranks and LA+SE showed the lowest mean value (0.013), followed by MM (0.015). While MM performed best in wavelengths up to around 782.8 nm, LA+SE performed best in larger wavelengths.

TABLE VII
MEAN ILLUMINATION CONDITION ($\cos\beta$), SLOPE [°], AND PERCENTAGE OF PIXELS WITH $\cos\beta < 0.45$ (SE) FOR THREE DIFFERENT SUBSETS (WHOLE SCENE, VEGETATION, BARE SOIL) AND TWO DATASETS (SENTINEL-2 AND APEX)

| | **Sentinel-2** | | | **APEX** | | |
|---|---|---|---|---|---|---|
| | $\cos\beta$ | Slope | SE | $\cos\beta$ | Slope | SE |
| **Whole scene** | 0.74 | 28.1 | 6.6 | 0.70 | 29.3 | 14.7 |
| **Vegetation** | 0.75 | 25.4 | 3.1 | 0.70 | 25.9 | 11.8 |
| **Bare soil** | 0.76 | 31.7 | 0.6 | 0.72 | 32.8 | 7.4 |

### C. Visual Impressions

Figs. 6 and 7 provide a visual comparison of a subset of the study site between different correction methods for both Sentinel-2 and APEX, respectively. While for Sentinel-2 (see Fig. 6), the general benefit of a topographic correction is clearly visible, only minor differences can be observed between the different correction methods. In the case of APEX (see Fig. 7), larger differences are visible. The LA correction, the SE correction, and hence, also LA+SE clearly show overcorrections in areas of low illumination condition, for example, the forest in the north-eastern part of the image. Here, MM and CC lead to more balanced results. These findings are even better observable in Figs. 8 and 9 in the Appendix, showing the differences in reflectance between no correction and the different correction methods for exemplary band 3 (559.8 nm).

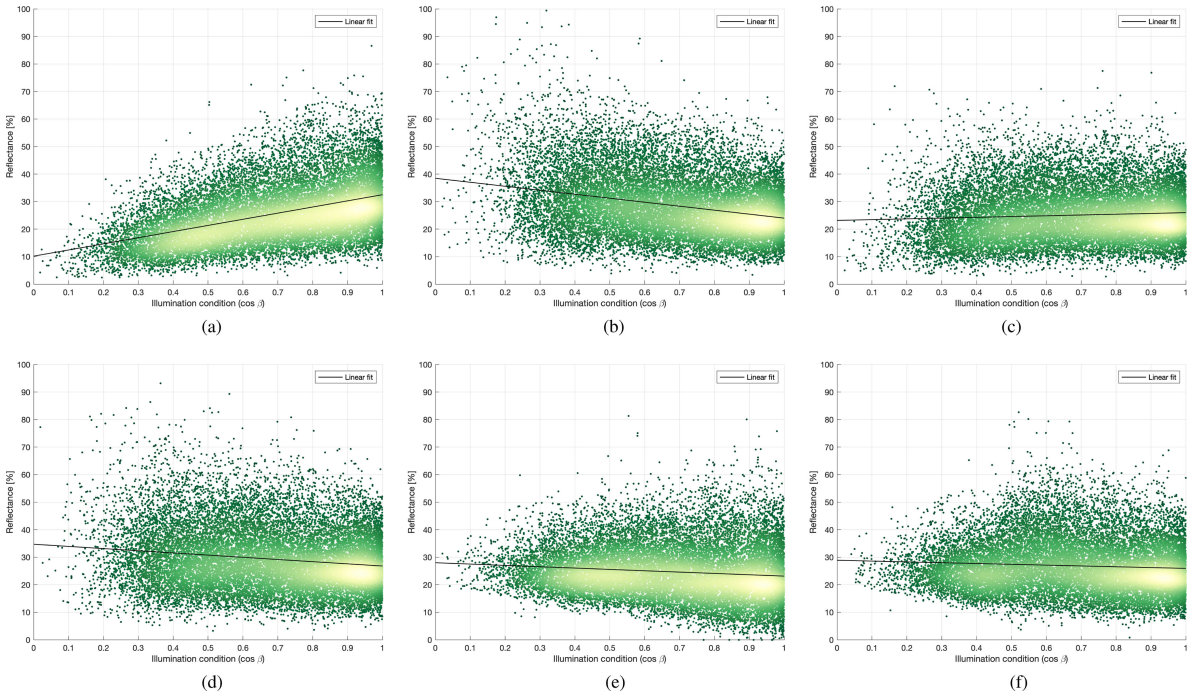


Fig. 5. Relation between reflectance in band 8 (832.8 nm) and illumination condition ($\cos\beta$) of APEX flight line A for different topographic correction methods. (a) no correction (NC). (b) Lambertian cosine correction (LA). (c) Modified Minnaert (MM). (d) C-correction (CC). (e) Statistical-Empirical (SE). (f) Merged LA+SE.

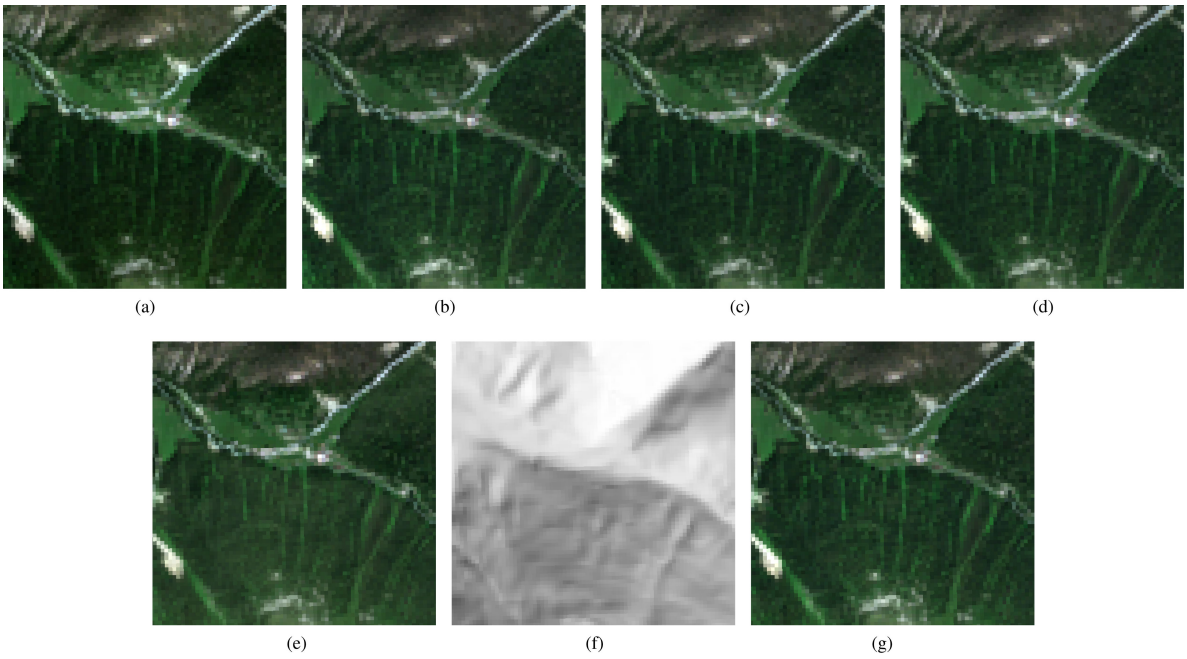


Fig. 6. True color representation ($R = 664.6$ nm, $G = 559.8$ nm, $B = 492.4$ nm) of a 1.5 km $\times$ 1.5 km subset of the Sentinel-2 scene. Oriented north (top) to south (bottom). Mean slope of the subset: 27.1°. (a) NC. (b) LA. (c) MM. (d) CC. (e) SE. (f) Illumination condition. (g) LA+SE.

## V. Discussion

We provide an evaluation of different topographic correction methods for multispectral spaceborne and airborne optical image data. This is obtained by comparing the reflectance data to the illumination condition $\cos\beta$. After a successful correction, the two should be independent. By applying the same correction methods and evaluation measures to airborne and spaceborne data, we investigate the influence of the spatial resolution on the correction of topography effects, and thus, the transferability of approaches originally designed for satellite data to spatially higher resolved airborne imagery. To the authors' best

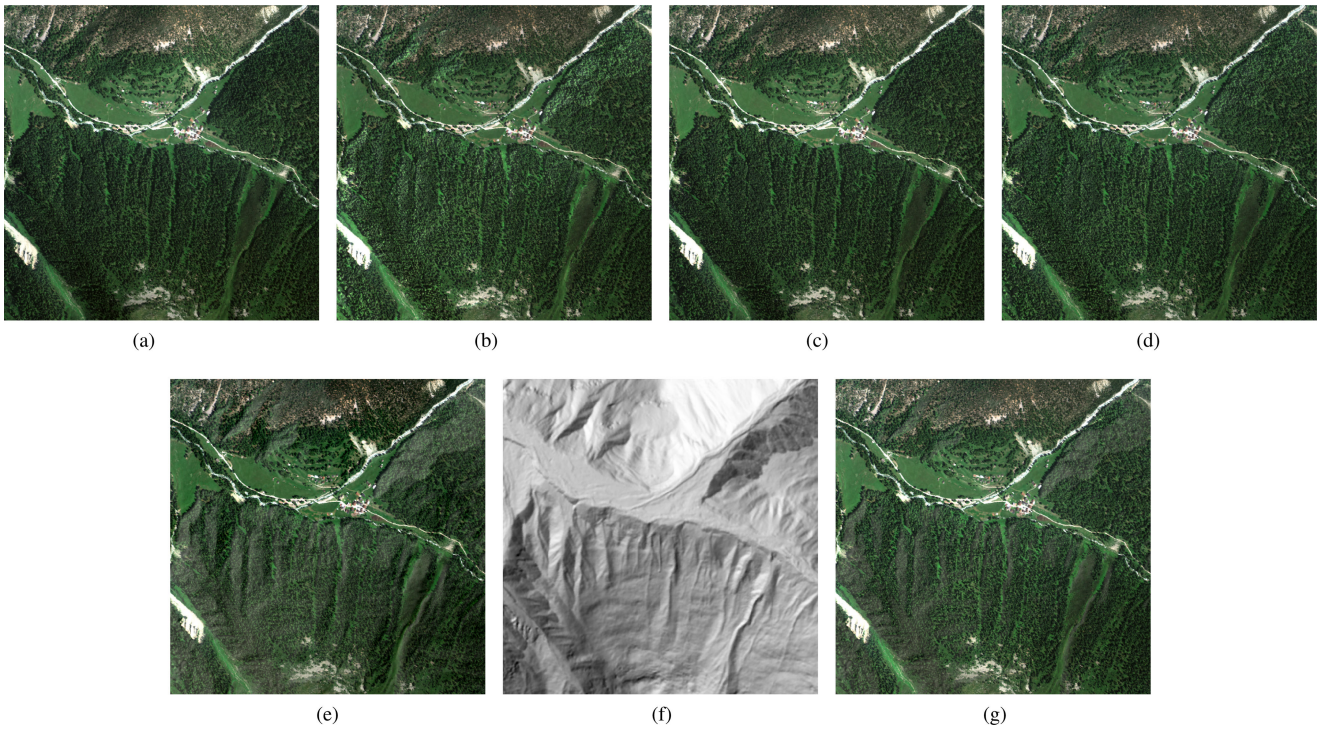


Fig. 7. True color representation ($R = 664.6$ nm, $G = 559.8$ nm, $B = 492.4$ nm) of a 1.5 km $\times$ 1.5 km subset of APEX flight line A. Oriented north (top) to south (bottom). Mean slope of the subset: 27.1°. (a) NC. (b) LA. (c) MM. (d) CC. (e) SE. (f) Illumination condition. (g) LA+SE.

knowledge, this is the first study of this issue. In addition, we propose a new merged physical-empirical correction method, based on a Lambertian physical correction complemented by a semiempirical correction for faintly illuminated areas.

### A. *Quality of the Methods*

In the case of Sentinel-2, the well-described SE and MM methods showed the best results in all analyzed subsets, however depending on wavelength. In the visible wavelengths up to band 5 (704.1 nm), SE clearly performed best while at the same time MM showed quite weak results. From band 6 (740.5 nm) onward, this changes to the opposite. Here, MM distinctly performed best and SE showed rather poor results. This switch from SE to MM is related to a change in the wavelength-dependent exponent $b_i$ for the calculation of MM [see (4)] after 720 nm. A slight alteration of $b_i$ below 720 nm could improve the numbers of MM and lead to more consistent results throughout all wavelengths. Some further variance in results could be related to the three different spatial resolutions (10 m, 20 m, 60 m) processed with 20 m and a corresponding DEM. Especially the 10 m bands might improve with an equally resolved DEM. The newly introduced merged LA+SE method provided good results, too, but was generally outperformed by SE and MM.

In the case of APEX, the situation looks slightly different. With regard to the whole scene, the new LA+SE method distinctly performed best, except for bands 2 and 3 (492.4 nm and 559.8 nm). MM and SE provide good results too. They generally score second or third best, but are outperformed by LA+SE. In the vegetation subset, however, MM clearly delivers better results than LA+SE. In the bare soil subset, LA+SE and MM are almost equal: while MM is superior in the lower wavelengths up to 832.8 nm, LA+SE is better in the higher wavelengths.

The results obtained for the Sentinel-2 data coincide with [12] and [13], who also observed that in many cases SE performs best with satellite data. The new LA+SE method does not lead to an improvement. This could be related to the topography of the respective subsets. Only 6.6% (whole scene), 3.1% (vegetation), and 0.6% (bare soil) of the pixels are subject to an illumination condition smaller than 0.45 and are, thus, corrected with SE in the LA+SE approach (see Table VII). This leads to a Lambertian cosine correction in a vast majority of the pixels and, thus, to a result not much different from the pure LA. This is slightly different in the case of APEX. Here, up to 14.7% of the pixels have a $\cos\beta$ below 0.45 and are thus corrected with SE.

A visual comparison of different corrections of the Sentinel-2 scene (see Fig. 6 and Section IV-C) reveals a distinct improvement compared to the uncorrected scene, but only minor differences between the different correction methods. This reflects the small differences between the four methods in the wavelength-normalized linear fit and the $R^2$ value (see Tables III and IV). Between the differently corrected APEX images (see Fig. 7, and Fig. 9 in the Appendix), however, larger differences are visible. The Lambertian cosine correction leads, as expected [see (2)], to unreasonably high reflectance values in areas of low illumination conditions, e.g., in the forest area in the north eastern part of the image. The SE and, thus, also the LA+SE corrections also do not provide a satisfactory result. In the same forest area, clear overcorrections are visible in the SE corrected image, which are propagated into the LA+SE corrected image where the illumination condition lies below 0.45. These areas

with overcorrections can be recognised in blue, i.e., areas with higher reflectance after correction, in Fig. 9 in the Appendix.

### *B. Transferability From Spaceborne to Airborne Data*

Our analysis on the transferability of topographic correction methods from spaceborne to airborne optical data is largely an issue of coarse versus high spatial resolution in the respective datasets.

Airborne sensors having similar ground spatial resolution can be used as comparison base to high resolution spaceborne sensors (such as WorldView, Pleiades, etc.). However, due to different illumination and observation angle configurations, it is expected that residual differences in anisotropic behavior (i.e., volumetric, geometric, and isotropic scattering) as well as path scattered radiance exist. In a first approximation, we assume only minor differences, but recommend in future refined experiments to quantify those differences, allowing large scale improvements when using SE corrections.

The higher spatial resolution of the airborne imagery leads to various effects on the topographic correction that do not occur in the spaceborne case. Due to the higher resolution, a larger contribution of cast shadows to the imagery emerges as more single pixels are fully shaded. This can be observed in Fig. 7, where cast shadows of individual trees are well visible in the forest. This has an impact on the image statistics (i.e., the scene-average TOA radiance or reflectance) used in the SE method [see (7)]. The dark shadows lead to an underestimation of the general image brightness. This results in a too strong correction in areas of low illumination condition and could explain the overcorrections observed in SE and LA+SE and mentioned in Section V-A.

Furthermore, there is a natural variation of vegetation brightness between northern and southern slopes in this summer time data acquisition—southernly exposed areas are supposedly dried out and, therefore, show higher reflectance in the visible part of the spectrum whereas the near infrared is less affected. The effect is more pronounced for the high resolution data as the variation of reflectance values is higher there, resulting in very dark pixels being enhanced to a statistical average. The SE method tries to adjust these differences to a common brightness, resulting in unnaturally bright northern slopes after the correction. The evaluation of such a correction shows favorable statistical results as the brightness between expositions does no longer vary, whereas indeed unnatural reflectance values have been produced.

Another difficulty only affecting high resolution imagery is the appropriate preprocessing of the DEM: the calculated illumination for a high-accuracy DEM shows natural structures which are masked by the vegetation and can not be seen in the real imagery [compare Fig. 7(f)]. This may lead to small scale overcorrections in the resulting imagery, which may be more pronounced in a stronger correction such as the SE approach [image (e) in Fig. 7].

### *C. BRDF Considerations*

The reflectance behavior of surfaces depends on the direction of the incident illumination source and the observation direction. It can be described by the BRDF. However, this quantity cannot be derived from a single scene acquisition, but would require *a priori* knowledge of the BRDF for each pixel. This information is not readily available for natural objects. Therefore, the surfaces are first assumed to be Lambertian with a spectral reflectance $\rho(\lambda)$ and only empirical topographic corrections as outlined herein can be applied. With these corrections, the incidence BRDF can only be roughly approximated. Even if the retrieval of atmospheric parameters would be perfect, an accurate estimation of the neighboring effects ($L_a, E_d^*, E_t, L_t$) is a great challenge, because these quantities depend themselves on the target BRDF and they constitute a closed-loop system complicating the solution of the radiative transfer. Each iteration step updates the individual pixel reflectance value according to the surrounding effects. Theoretically, the BRDF of all pixels in the line-of-sight of an individual target pixel is required for an accurate solution of (8)–(13), but this information is not available in practice, and this will cause an inherent loss of accuracy.

As the engaged empirical topographic corrections are limited, a fully bidirectional BRDF correction based on a land cover specific physical model parametrisation is a potential solution.

Such developments have been published in the past to (i) map forest heterogeneity [35]–[37], (ii) characterise various surface scattering types (i.e., land cover types) [38], [39], and (iii) correct BRDF effects in forest canopies [40]. For alpine landscapes, a respective BRDF model has to be adapted to the predominant land cover types. Using the approach as implemented in the BREFCOR method [41] in combination with the topographic angular variations is a promising way to further improve topographic corrections in a more physical way.

## VI. Conclusion

The presented analyses have shown that topographic correction can successfully be applied to both satellite and airborne imagery whereas differences in the preferable method are immanent. The readily available methods are now in a mature state and are widely accepted for operational use. In general, it can be concluded that the combination of the Lambertian cosine atmospheric/topographic correction for relatively flat areas with the SE approach for incidence angles exceeding about 60° leads to good corrections, specifically for satellite imagery.

For airborne high resolution data, however, problems with SE adjustments are becoming more visible. Using SE methods can lead to significant problems if only small scale imagery are analyzed, where certain slope expositions may be statistically underrepresented or if the surface cover type shows natural variations of reflectances in dependence of the solar exposition. In such cases, the MM method often can be recommended over SE approaches. Similar insights can be expected for high resolution spaceborne sensors, although some residual differences in anisotropic behavior and path scattered radiance may exist.

The development of a BRDF model based scene correction has only started now but it is expected that only such methods could further improve topographic correction. They may solve for object-specific differences in bidirectional behavior and due to relying on physical models for a more consistent topographic correction.

## APPENDIX
## ADDITIONAL RESULTS

TABLE VIII
WAVELENGTH-NORMALIZED SLOPE OF A LINEAR FIT BETWEEN REFLECTANCE AND ILLUMINATION CONDITION FOR 13 SENTINEL-2 BANDS, SUBSET TO VEGETATION

| | Wavelength [nm] | | | | | | | | | | | | | |
|---|---|---|---|---|---|---|---|---|---|---|---|---|---|---|
| | **442.7** | **492.4** | **559.8** | **664.6** | **704.1** | **740.5** | **782.8** | **832.8** | **864.7** | **945.1** | **1373.5** | **1613.7** | **2202.4** | **Mean** |
| **NC** | 1.449 | 1.298 | 0.905 | 1.243 | 0.849 | 0.652 | 0.649 | 0.661 | 0.672 | 0.642 | 0.786 | 0.917 | 1.004 | 0.902 |
| **LA** | 0.378 | 0.473 | 0.618 | 0.361 | 0.609 | 0.723 | 0.713 | 0.693 | 0.677 | 0.664 | 0.560 | 0.465 | 0.432 | 0.567 |
| **MM** | 0.323 | 0.211 | **0.063** | 0.316 | **0.067** | 0.406 | **0.397** | **0.378** | **0.363** | **0.350** | **0.245** | **0.149** | 0.106 | **0.259** |
| **CC** | 0.397 | **0.100** | 0.100 | 0.179 | 0.164 | **0.406** | 0.423 | 0.430 | 0.411 | 0.395 | 0.281 | 0.176 | **0.010** | 0.267 |
| **SE** | 0.078 | 0.507 | 0.569 | 0.428 | 0.488 | 0.601 | 0.622 | 0.612 | 0.593 | 0.585 | 0.484 | 0.390 | 0.333 | 0.484 |
| **LA+SE** | **0.022** | 0.237 | 0.368 | **0.133** | 0.348 | 0.487 | 0.490 | 0.476 | 0.460 | 0.457 | 0.344 | 0.241 | 0.175 | 0.326 |

Lowest values per wavelength are highlighted with bold letters.

TABLE IX
$R^2$ OF A LINEAR REGRESSION BETWEEN REFLECTANCE AND ILLUMINATION CONDITION FOR 13 SENTINEL-2 BANDS, SUBSET TO VEGETATION

| | Wavelength [nm] | | | | | | | | | | | | | |
|---|---|---|---|---|---|---|---|---|---|---|---|---|---|---|
| | **442.7** | **492.4** | **559.8** | **664.6** | **704.1** | **740.5** | **782.8** | **832.8** | **864.7** | **945.1** | **1373.5** | **1613.7** | **2202.4** | **Mean** |
| **NC** | 0.061 | 0.149 | 0.103 | 0.131 | 0.103 | 0.080 | 0.083 | 0.084 | 0.091 | 0.094 | 0.122 | 0.130 | 0.145 | 0.106 |
| **LA** | 0.011 | 0.031 | 0.059 | 0.015 | 0.059 | 0.104 | 0.105 | 0.098 | 0.098 | 0.105 | 0.068 | 0.038 | 0.030 | 0.063 |
| **MM** | 0.008 | 0.007 | **0.001** | 0.012 | **0.001** | 0.035 | **0.035** | **0.031** | **0.030** | **0.031** | **0.014** | **0.004** | 0.002 | **0.016** |
| **CC** | 0.013 | **0.002** | 0.002 | 0.004 | 0.005 | **0.035** | 0.039 | 0.040 | 0.038 | 0.039 | 0.018 | 0.006 | **0.000** | 0.018 |
| **SE** | 0.000 | 0.039 | 0.052 | 0.022 | 0.040 | 0.072 | 0.079 | 0.075 | 0.073 | 0.079 | 0.050 | 0.027 | 0.019 | 0.048 |
| **LA+SE** | **0.000** | 0.009 | 0.023 | **0.002** | 0.021 | 0.051 | 0.054 | 0.050 | 0.049 | 0.053 | 0.028 | 0.011 | 0.005 | 0.027 |

Lowest values per wavelength are highlighted with bold letter.

TABLE X
WAVELENGTH-NORMALIZED SLOPE OF A LINEAR FIT BETWEEN REFLECTANCE AND ILLUMINATION CONDITION FOR 13 SENTINEL-2 BANDS, SUBSET TO BARE SOIL

| | Wavelength [nm] | | | | | | | | | | | | | |
|---|---|---|---|---|---|---|---|---|---|---|---|---|---|---|
| | **442.7** | **492.4** | **559.8** | **664.6** | **704.1** | **740.5** | **782.8** | **832.8** | **864.7** | **945.1** | **1373.5** | **1613.7** | **2202.4** | **Mean** |
| **NC** | 0.397 | 0.577 | 0.565 | 0.555 | 0.579 | 0.638 | 0.646 | 0.654 | 0.666 | 0.633 | 0.649 | 0.657 | 0.666 | 0.606 |
| **LA** | 1.018 | 0.855 | 0.854 | 0.867 | 0.831 | 0.748 | 0.730 | 0.715 | 0.692 | 0.669 | 0.671 | 0.673 | 0.685 | 0.770 |
| **MM** | 0.583 | 0.414 | 0.418 | 0.432 | 0.402 | **0.327** | **0.312** | **0.299** | **0.279** | **0.268** | **0.274** | **0.277** | 0.285 | **0.352** |
| **CC** | 0.230 | **0.228** | 0.331 | 0.330 | 0.412 | 0.449 | 0.455 | 0.464 | 0.438 | 0.417 | 0.418 | 0.418 | 0.325 | 0.378 |
| **SE** | **0.126** | 0.236 | **0.097** | **0.181** | **0.072** | 0.752 | 0.943 | 0.996 | 1.006 | 0.968 | 0.576 | 0.358 | **0.015** | 0.486 |
| **LA+SE** | 0.671 | 0.495 | 0.524 | 0.528 | 0.544 | 0.577 | 0.593 | 0.590 | 0.579 | 0.578 | 0.541 | 0.520 | 0.475 | 0.555 |

Lowest values per wavelength are highlighted with bold letters.

TABLE XI
$R^2$ OF A LINEAR REGRESSION BETWEEN REFLECTANCE AND ILLUMINATION CONDITION FOR 13 SENTINEL-2 BANDS, SUBSET TO BARE SOIL

| | Wavelength [nm] | | | | | | | | | | | | | |
|---|---|---|---|---|---|---|---|---|---|---|---|---|---|---|
| | **442.7** | **492.4** | **559.8** | **664.6** | **704.1** | **740.5** | **782.8** | **832.8** | **864.7** | **945.1** | **1373.5** | **1613.7** | **2202.4** | **Mean** |
| **NC** | 0.023 | 0.032 | 0.038 | 0.041 | 0.052 | 0.069 | 0.077 | 0.077 | 0.090 | 0.111 | 0.112 | 0.093 | 0.110 | 0.071 |
| **LA** | 0.153 | 0.076 | 0.088 | 0.096 | 0.103 | 0.092 | 0.095 | 0.090 | 0.094 | 0.114 | 0.111 | 0.092 | 0.108 | 0.101 |
| **MM** | 0.061 | 0.020 | 0.024 | 0.027 | 0.027 | **0.020** | **0.019** | **0.017** | **0.017** | **0.020** | **0.021** | **0.017** | 0.021 | **0.024** |
| **CC** | 0.010 | **0.006** | 0.015 | 0.016 | 0.029 | 0.037 | 0.041 | 0.042 | 0.042 | 0.049 | 0.048 | 0.039 | 0.028 | 0.031 |
| **SE** | **0.003** | 0.007 | **0.001** | **0.005** | **0.001** | 0.097 | 0.154 | 0.165 | 0.185 | 0.218 | 0.088 | 0.029 | **0.000** | 0.073 |
| **LA+SE** | 0.083 | 0.030 | 0.039 | 0.041 | 0.051 | 0.063 | 0.071 | 0.069 | 0.074 | 0.096 | 0.081 | 0.060 | 0.058 | 0.063 |

Lowest values per wavelength are highlighted with bold letters.

TABLE XII
WAVELENGTH-NORMALIZED SLOPE OF A LINEAR FIT BETWEEN REFLECTANCE AND ILLUMINATION CONDITION FOR 13 APEX BANDS, AVERAGED OVER THREE FLIGHT LINES AND SUBSET TO VEGETATION

| | Wavelength [nm] | | | | | | | | | | | | | |
|---|---|---|---|---|---|---|---|---|---|---|---|---|---|---|
| | **442.7** | **492.4** | **559.8** | **664.6** | **704.1** | **740.5** | **782.8** | **832.8** | **864.7** | **945.1** | **1373.5** | **1613.7** | **2202.4** | **Mean** |
| **NC** | 1.160 | 0.849 | 0.734 | 0.909 | 0.752 | 0.665 | 0.680 | 0.694 | 0.704 | 0.744 | 0.858 | 0.993 | 0.985 | 0.825 |
| **LA** | 0.737 | 0.865 | 0.886 | 0.730 | 0.812 | 0.758 | 0.708 | 0.679 | 0.656 | 0.606 | 0.554 | 0.495 | 0.612 | 0.700 |
| **MM** | 0.464 | 0.331 | **0.290** | 0.439 | **0.341** | **0.232** | **0.189** | **0.162** | **0.141** | **0.094** | **0.037** | **0.054** | **0.072** | **0.219** |
| **CC** | **0.105** | **0.209** | 0.297 | **0.188** | 0.373 | 0.492 | 0.496 | 0.497 | 0.499 | 0.466 | 0.380 | 0.281 | 0.205 | 0.345 |
| **SE** | 1.679 | 1.402 | 1.005 | 1.409 | 0.722 | 0.291 | 0.243 | 0.230 | 0.224 | 0.211 | 0.326 | 0.463 | 0.790 | 0.692 |
| **LA+SE** | 0.564 | 0.536 | 0.450 | 0.506 | 0.358 | 0.265 | 0.246 | 0.236 | 0.232 | 0.208 | 0.183 | 0.154 | 0.262 | 0.323 |

Lowest values per wavelength are highlighted with bold letters.

TABLE XIII
$R^2$ OF A LINEAR REGRESSION BETWEEN REFLECTANCE AND ILLUMINATION CONDITION FOR 13 APEX BANDS, AVERAGED OVER THREE FLIGHT LINES AND SUBSET TO VEGETATION

| | Wavelength [nm] | | | | | | | | | | | | | |
|---|---|---|---|---|---|---|---|---|---|---|---|---|---|---|
| | **442.7** | **492.4** | **559.8** | **664.6** | **704.1** | **740.5** | **782.8** | **832.8** | **864.7** | **945.1** | **1373.5** | **1613.7** | **2202.4** | **Mean** |
| **NC** | 0.128 | 0.132 | 0.109 | 0.142 | 0.107 | 0.090 | 0.093 | 0.098 | 0.102 | 0.110 | 0.142 | 0.159 | 0.167 | 0.122 |
| **LA** | 0.063 | 0.130 | 0.144 | 0.093 | 0.118 | 0.116 | 0.105 | 0.100 | 0.095 | 0.086 | 0.070 | 0.046 | 0.072 | 0.095 |
| **MM** | 0.036 | 0.030 | 0.023 | 0.042 | **0.027** | **0.012** | **0.008** | **0.006** | **0.005** | **0.002** | **0.001** | **0.001** | **0.002** | **0.015** |
| **CC** | **0.003** | **0.011** | **0.022** | **0.009** | 0.029 | 0.050 | 0.051 | 0.051 | 0.052 | 0.048 | 0.032 | 0.015 | 0.009 | 0.029 |
| **SE** | 0.259 | 0.280 | 0.176 | 0.265 | 0.092 | 0.017 | 0.012 | 0.011 | 0.010 | 0.009 | 0.022 | 0.036 | 0.105 | 0.099 |
| **LA+SE** | 0.045 | 0.066 | 0.048 | 0.057 | 0.028 | 0.016 | 0.014 | 0.013 | 0.013 | 0.011 | 0.009 | 0.005 | 0.016 | 0.026 |

Lowest values per wavelength are highlighted with bold letters.

TABLE XIV
WAVELENGTH-NORMALIZED SLOPE OF A LINEAR FIT BETWEEN REFLECTANCE AND ILLUMINATION CONDITION FOR 13 APEX BANDS, AVERAGED OVER THREE FLIGHT LINES AND SUBSET TO BARE SOIL

| | Wavelength [nm] | | | | | | | | | | | | | |
|---|---|---|---|---|---|---|---|---|---|---|---|---|---|---|
| | **442.7** | **492.4** | **559.8** | **664.6** | **704.1** | **740.5** | **782.8** | **832.8** | **864.7** | **945.1** | **1373.5** | **1613.7** | **2202.4** | **Mean** |
| **NC** | 0.704 | 0.705 | 0.732 | 0.760 | 0.796 | 0.846 | 0.864 | 0.881 | 0.892 | 0.926 | 0.936 | 0.943 | 0.930 | 0.840 |
| **LA** | 0.755 | 0.725 | 0.665 | 0.632 | 0.580 | 0.505 | 0.476 | 0.452 | 0.430 | 0.440 | 0.408 | 0.389 | 0.456 | 0.532 |
| **MM** | **0.071** | **0.071** | **0.063** | **0.068** | 0.094 | **0.160** | **0.186** | **0.207** | 0.226 | 0.217 | 0.235 | 0.247 | 0.190 | **0.157** |
| **CC** | 0.327 | 0.292 | 0.262 | 0.275 | 0.278 | 0.271 | 0.265 | 0.256 | 0.249 | 0.239 | 0.227 | 0.219 | 0.195 | 0.258 |
| **SE** | 0.172 | 0.173 | 0.137 | 0.183 | **0.088** | 0.277 | 0.352 | 0.373 | 0.388 | 0.372 | 0.179 | 0.140 | 0.172 | 0.231 |
| **LA+SE** | 0.131 | 0.137 | 0.139 | 0.117 | 0.137 | 0.205 | 0.216 | 0.213 | **0.211** | **0.199** | **0.124** | **0.121** | **0.098** | 0.158 |

Lowest values per wavelength are highlighted with bold letters.

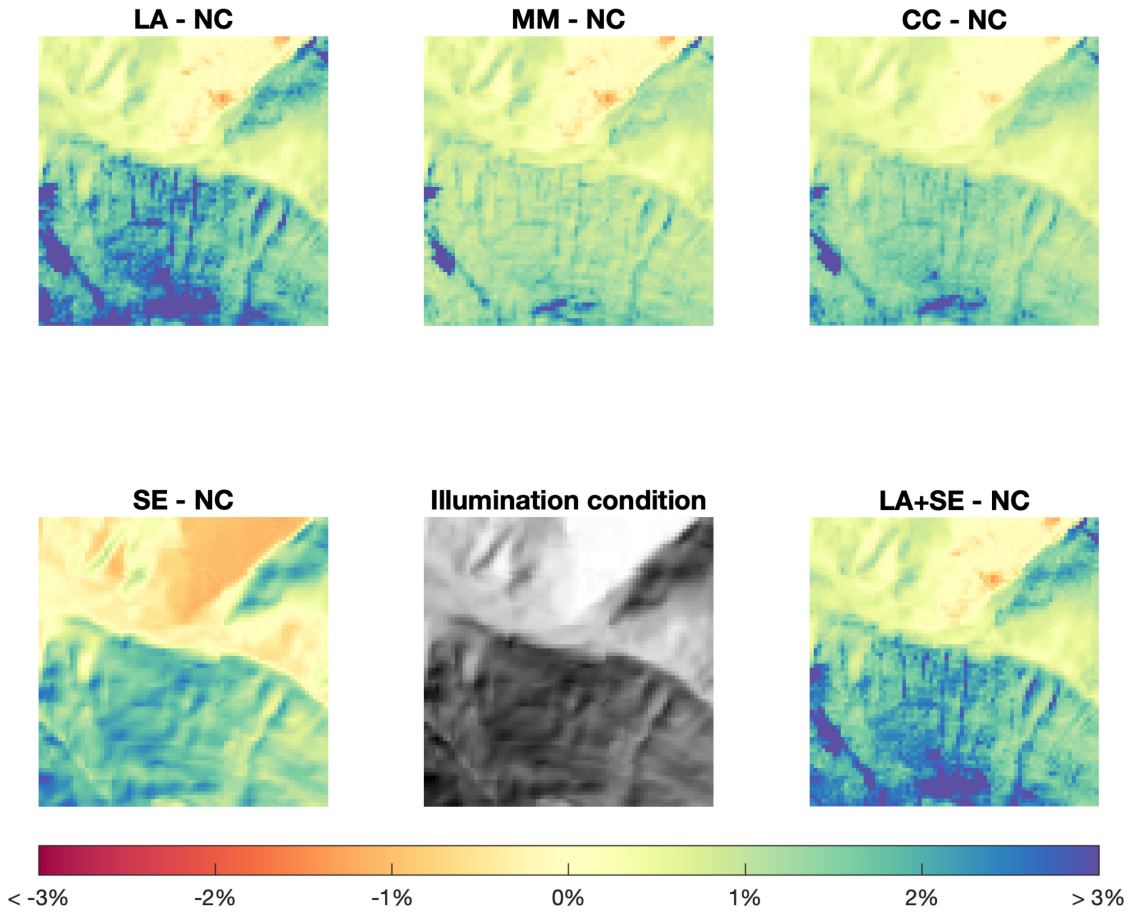


Fig. 8. Differences in reflectance between no correction (NC) and Lambertian correction (LA), Modified Minnaert correction (MM), C-correction (CC), Statistical-Empirical correction (SE), and merged LA+SE correction respectively for Sentinel-2 band 3 (559.8 nm). Positive (blue) values indicate a higher reflectance after correction, negative (red) values indicate a lower reflectance after correction. The illumination condition is shown for reference.

TABLE XV
$R^2$ OF A LINEAR REGRESSION BETWEEN REFLECTANCE AND ILLUMINATION CONDITION FOR 13 APEX BANDS, AVERAGED OVER THREE FLIGHT LINES AND SUBSET TO BARE SOIL

| | Wavelength [nm] | | | | | | | | | | | | | |
|---|---|---|---|---|---|---|---|---|---|---|---|---|---|---|
| | **442.7** | **492.4** | **559.8** | **664.6** | **704.1** | **740.5** | **782.8** | **832.8** | **864.7** | **945.1** | **1373.5** | **1613.7** | **2202.4** | **Mean** |
| **NC** | 0.121 | 0.147 | 0.173 | 0.181 | 0.200 | 0.226 | 0.235 | 0.243 | 0.249 | 0.258 | 0.254 | 0.223 | 0.248 | 0.212 |
| **LA** | 0.152 | 0.160 | 0.148 | 0.130 | 0.114 | 0.091 | 0.082 | 0.076 | 0.069 | 0.078 | 0.062 | 0.047 | 0.071 | 0.098 |
| **MM** | **0.004** | **0.003** | **0.002** | **0.003** | **0.006** | **0.014** | **0.018** | 0.022 | 0.025 | 0.025 | 0.027 | 0.025 | 0.018 | 0.015 |
| **CC** | 0.041 | 0.038 | 0.036 | 0.038 | 0.037 | 0.030 | 0.028 | 0.027 | 0.025 | 0.025 | 0.023 | 0.019 | 0.017 | 0.030 |
| **SE** | 0.017 | 0.018 | 0.014 | 0.018 | 0.006 | 0.031 | 0.046 | 0.051 | 0.055 | 0.054 | 0.015 | 0.008 | 0.018 | 0.027 |
| **LA+SE** | 0.010 | 0.012 | 0.011 | 0.008 | 0.010 | 0.020 | 0.022 | **0.021** | **0.021** | **0.020** | **0.009** | **0.006** | **0.004** | **0.013** |

Lowest values per wavelength are highlighted with bold letters.

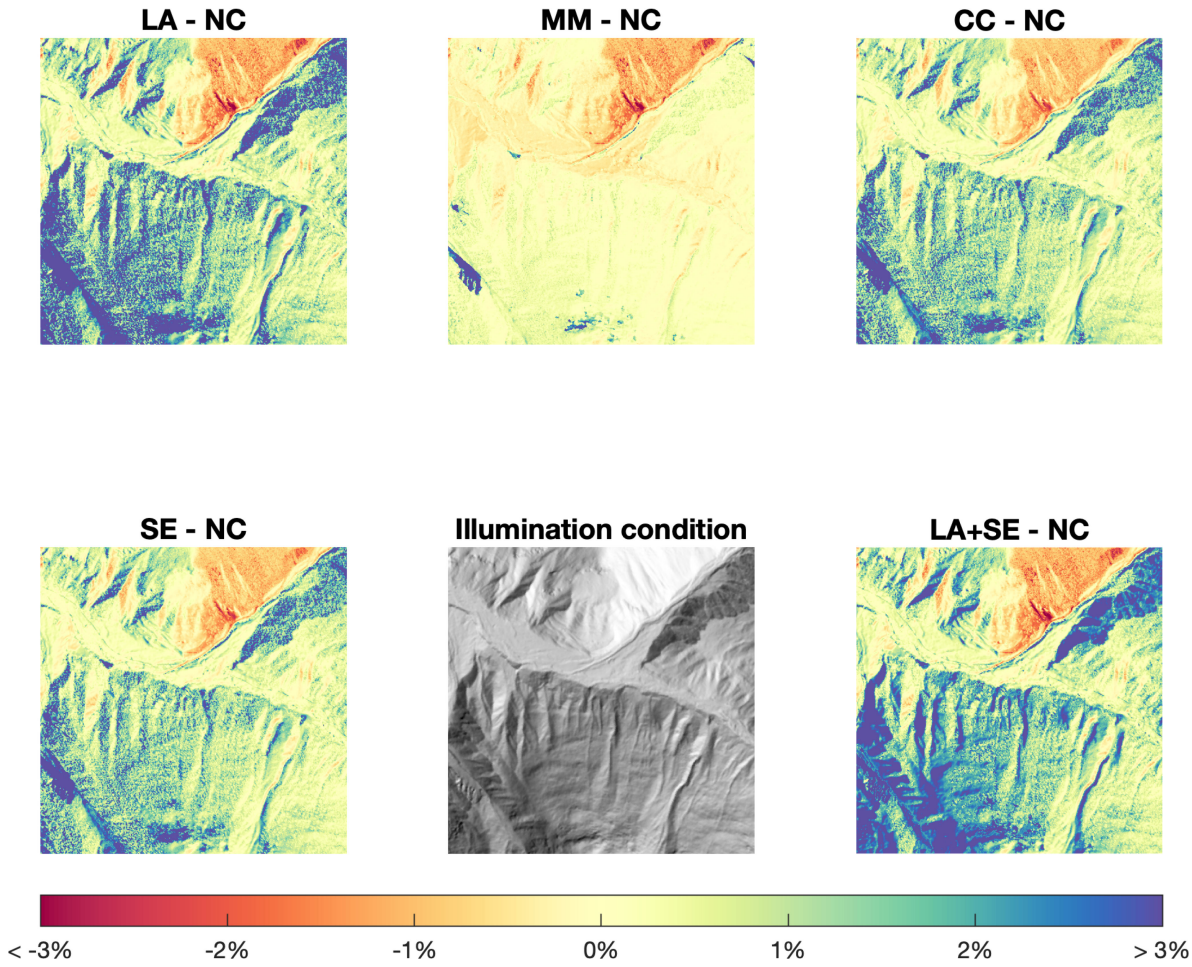


Fig. 9. Differences in reflectance between no correction (NC) and Lambertian correction (LA), Modified Minnaert correction (MM), C-correction (CC), Statistical-Empirical correction (SE), and merged LA+SE correction, respectively for APEX band 3 (559.8 nm). Positive (blue) values indicate a higher reflectance after correction, negative (red) values indicate a lower reflectance after correction. The illumination condition is shown for reference.

## REFERENCES

[1] F. E. Nicodemus, J. C. Richmond, J. J. Hsia, I. W. Ginsberg, and T. Limperis, *Geometrical Considerations and Nomenclature for Reflectance*. U.S. Department of Commerce, National Bureau of Standards, Gaithersburg, MD, USA, 1977.

[2] R. Richter, T. Kellenberger, and H. Kaufmann, "Comparison of topographic correction methods," *Remote Sens.*, vol. 1, no. 3, pp. 184–196, 2009.

[3] J. A. Smith, T. L. Lin, and K. J. Ranson, "The Lambertian assumption and Landsat data," *Photogrammetric Eng. Remote Sens.*, vol. 46, no. 9, pp. 1183–1189, 1980.

[4] B. N. Holben and C. Justice, "The topographic effect on spectral response from nadir-pointing sensors," *Photogrammetric Eng. Remote Sens.*, vol. 46, no. 9, pp. 1191–1200, 1980.

[5] C. O. Justice, S. W. Wharton, and B. N. Holben, "Application of digital terrain data to quantify and reduce the topographic effect on Landsat data," *Int. J. Remote Sens.*, vol. 2, no. 3, pp. 213–230, 1981.

[6] P. M. Teillet, B. Guindon, and D. G. Goodenough, "On the slope-aspect correction of multispectral scanner data," *Can. J. Remote Sens.*, vol. 8, no. 2, pp. 84–106, 1982.

[7] C. Proy, D. Tanré, and P. Y. Deschamps, "Evaluation of topographic effects in remotely sensed data," *Remote Sens. Environ.*, vol. 30, no. 1, pp. 21–32, 1989.

[8] C. Conese, A. Gilabert, P. Maselli, and L. Bottai, "Topographic normalization of TM scenes through the use of an atmospheric correction method and digital terrain models," *Photogrammetric Eng. Remote Sens.*, vol. 25, no. 12, pp. 1745–1753, 1993.
[9] S. Sandmeier and K. Itten, "A physically-based model to correct atmospheric and illumination effects in optical satellite data of rugged terrain," *IEEE Trans. Geosci. Remote Sens.*, vol. 35, no. 3, pp. 708–717, May 1997.
[10] R. Richter, "Correction of satellite imagery over mountainous terrain," *Appl. Opt.*, vol. 37, no. 18, pp. 4004–4015, 1998.
[11] R. Richter and D. Schläpfer, "Geo-atmospheric processing of airborne imaging spectrometry data. Part 2: Atmospheric/topographic correction," *Int. J. Remote Sens.*, vol. 23, no. 13, pp. 2631–2649, 2002.
[12] I. Sola, M. González-Audícana, and J. Álvarez-Mozos, "Multi-criteria evaluation of topographic correction methods," *Remote Sens. Environ.*, vol. 184, pp. 247–262, 2016.
[13] S. Hantson and E. Chuvieco, "Evaluation of different topographic correction methods for Landsat imagery," *Int. J. Appl. Earth Observ. Geoinf.*, vol. 13, no. 5, pp. 691–700, 2011.
[14] Z. Ma, G. Jia, M. E. Schaepman, and H. Zhao, "Uncertainty analysis for topographic correction of hyperspectral remote sensing images," *Remote Sens.*, vol. 12, no. 4, 2020, Art. no. 705.
[15] G. Yin, A. Li, W. Zhao, H. Jin, J. Bian, and S. Wu, "Modeling canopy reflectance over sloping terrain based on path length correction," *IEEE Trans. Geosci. Remote Sens.*, vol. 55, no. 8, pp. 4597–4609, Aug. 2017.
[16] F. Crameri, "Geodynamic diagnostics, scientific visualisation and StagLab 3.0," *Geosci. Model Develop.*, vol. 11, no. 6, pp. 2541–2562, 2018.
[17] M. Drusch *et al.*, "Sentinel-2: ESA's optical high-resolution mission for GMES operational services," *Remote Sens. Environ.*, vol. 120, pp. 25–36, 2012.
[18] R. Richter and D. Schläpfer, "Atmospheric and topographic correction (ATCOR theoretical background document)," DLR/ReSe, Cologne, Germany, Tech. Rep. DLR-IB 564-03/2019, 2019. [Online]. Available: https://www.rese-apps.com/pdf/atcor_ATBD.pdf
[19] M. E. Schaepman *et al.*, "Advanced radiometry measurements and Earth science applications with the Airborne Prism Experiment (APEX)," *Remote Sens. Environ.*, vol. 158, pp. 207–219, 2015.
[20] D. Schläpfer and R. Richter, "Geo-atmospheric processing of airborne imaging spectrometry data. Part 1: Parametric orthorectification," *Int. J. Remote Sens.*, vol. 23, no. 13, pp. 2609–2630, 2002.
[21] A. Hueni, *et al.*, "Structure, components, and interfaces of the airborne prism experiment (APEX) processing and archiving facility," *IEEE Trans. Geosci. Remote Sens.*, vol. 47, no. 1, pp. 29–43, Jan. 2009.
[22] A. Berk *et al.*, "MODTRAN5: A reformulated atmospheric band model with auxiliary species and practical multiple scattering options," in *Algorithms and Technologies for Multispectral, Hyperspectral, and Ultraspectral Imagery,* X. S. S. Shen and P. E. Lewis, Eds., vol. 5425, Bellingham, WA, USA: SPIE, 2004, pp. 341–347.
[23] D. Schläpfer, C. C. Borel, J. Keller, and K. I. Itten, "Atmospheric precorrected differential absorption technique to retrieve columnar water vapor," *Remote Sens. Environ.*, vol. 65, no. 3, pp. 353–366, 1998.
[24] A. Makarau, R. Richter, D. Schläpfer, and P. Reinartz, "APDA water vapor retrieval validation for Sentinel-2 imagery," *IEEE Geosci. Remote Sens. Lett.*, vol. 14, no. 2, pp. 227–231, Feb. 2017.
[25] D. Riano, E. Chuvieco, J. Salas, and I. Aguado, "Assessment of different topographic corrections in Landsat-TM data for mapping vegetation types (2003)," *IEEE Trans. Geosci. Remote Sens.*, vol. 41, no. 5, pp. 1056–1061, May 2003.
[26] M. Minnaert, "The reciprocity principle in lunar photometry," *Astrophys. J.*, vol. 93, pp. 403–410, 1941.
[27] K. Kriebel, "Measured spectral bidirectional reflection properties of four vegetated surfaces," *Appl. Opt.*, vol. 17, no. 2, pp. 253–259, 1978.
[28] C. Schaaf, X. Li, and A. Strahler, "Topographic effects on bidirectional and hemispherical reflectances calculated with a geometric-optical canopy model," *IEEE Trans. Geosci. Remote Sens.*, vol. 32, no. 6, pp. 1186–1193, Nov. 1994.
[29] F. Maignan, F.-M. Bréon, and R. Lacaze, "Bidirectional reflectance of Earth targets: Evaluation of analytical models using a large set of spaceborne measurements with emphasis on the Hot Spot," *Remote Sens. Environ.*, vol. 90, no. 2, pp. 210–220, 2004.
[30] F.-M. Bréon and E. Vermote, "Correction of MODIS surface reflectance time series for BRDF effects," *Remote Sens. Environ.*, vol. 125, pp. 1–9, 2012.
[31] J. Dozier, "Spectral signature of alpine snow cover from the Landsat thematic mapper," *Remote Sens. Environ.*, vol. 28, pp. 9–22, 1989.
[32] J. Dozier and T. H. Painter, "Multispectral and hyperspectral remote sensing of alpine snow properties," *Annu. Rev. Earth Planet. Sci.*, vol. 32, no. 1, pp. 465–494, 2004.
[33] J. Dozier, J. Bruno, and P. Downey, "A faster solution to the horizon problem," *Comput. Geosci.*, vol. 7, no. 2, pp. 145–151, 1981.
[34] J. E. Hay and D. C. McKay, "Estimating solar irradiance on inclined surfaces: A review and assessment of methodologies," *Int. J. Sol. Energy*, vol. 3, no. 4/5, pp. 203–240, 1985.
[35] J. Verrelst, M. E. Schaepman, B. Koetz, and M. Kneubühler, "Angular sensitivity analysis of vegetation indices derived from CHRIS/PROBA data," *Remote Sens. Environ.*, vol. 112, no. 5, pp. 2341–2353, 2008.
[36] J. Verrelst, M. E. Schaepman, and J. G. Clevers, "Spectrodirectional Minnaert-k retrieval using CHRIS/PROBA data," *Can. J. Remote Sens.*, vol. 36, no. 6, pp. 631–644, 2010.
[37] J. Verrelst, J. G. P. W. Clevers, and M. E. Schaepman, "Merging the Minnaert-k parameter with spectral unmixing to map forest heterogeneity with CHRIS/PROBA data," *IEEE Trans. Geosci. Remote Sens.*, vol. 48, no. 11, pp. 4014–4022, Nov. 2010.
[38] J. Weyermann, A. Damm, M. Kneubühler, and M. E. Schaepman, "Correction of reflectance Anisotropy effects of vegetation on airborne spectroscopy data and derived products," *IEEE Trans. Geosci. Remote Sens.*, vol. 52, no. 1, pp. 616–627, Jan. 2014.
[39] J. Weyermann, M. Kneubühler, D. Schläpfer, and M. E. Schaepman, "Minimizing reflectance anisotropy effects in airborne spectroscopy data using Ross-Li model inversion with continuous field land cover stratification," *IEEE Trans. Geosci. Remote Sens.*, vol. 53, no. 11, pp. 5814–5823, Nov. 2015.
[40] W. Jia, Y. Pang, R. Tortini, D. Schläpfer, Z. Li, and J.-L. Roujean, "A kernel-driven BRDF approach to correct airborne hyperspectral imagery over forested areas with rugged topography," *Remote Sens.*, vol. 12, no. 3, 2020, Art. no. 432.
[41] D. Schläpfer, R. Richter, and T. Feingersh, "Operational BRDF effects correction for wide-field-of-view optical scanners (BREFCOR)," *IEEE Trans. Geosci. Remote Sens.*, vol. 53, no. 4, pp. 1855–1864, Apr. 2015.

**Marius Vögtli** received the B.Sc. and M.Sc. degrees in geography, in 2016 and 2018, respectively, from the University of Zurich, Zurich, Switzerland, where he is currently working toward the Ph.D. degree in Remote Sensing with the Remote Sensing Laboratories.

His research interests include the processing and the analysis of airborne imaging spectroscopy data, and the retrieval of vegetation traits to describe natural ecosystems.

**Daniel Schläpfer** (Member, IEEE) received the M.Sc. degree in geography and atmospheric physics and the Ph.D. (Dr. sc. nat.) degree in remote sensing from the University of Zurich, Zurich, Switzerland, in 1994 and 1998, respectively, and the Teaching Professor degree in physics from the Education Department of Canton, St. Gallen, Switzerland, in 2009.

From 1998 to 2008, he was a Research Scientist with the Remote Sensing Laboratories, University of Zurich. He is currently with ReSe Applications LLC, Wil, Switzerland. He holds a physics teaching position with Kantonsschule, Wil, Switzerland. His research interests include the geometric preprocessing of airborne scanner data on the basis of the PARGE software, the application of radiative transfer models in imaging spectroscopy, and the advancement of radiometric and atmospheric compensation in the framework of the ATCOR atmospheric correction solution.

**Rudolf Richter** received the M.Sc. (Diplom) in physics from the Technical University of Munich, Germany, in 1973 and the Ph.D. (Dr. Ing.) degree in engineering from the Technical University of Dresden in 1991. He is a DLR Senior Scientist actively involved in optical remote sensing research and development. His areas of interest include atmospheric modeling, atmospheric and topographic correction, and simulation of airborne/spaceborne multispectral and hyperspectral instruments. He holds four patents related to optical remote sensing. He developed the ATCOR model, one of the standard codes for atmospheric and topographic correction of multi-/hyperspectral imagery used at universities, research laboratories, and industry. He is currently a Reviewer for seven scientific journals on remote sensing and has authored or coauthored more than 50 research publications in refereed journals on processing of multispectral and hyperspectral imagery. Since his retirement he works as consultant for DLR and ReSe Applications.

**Andreas Hueni** (Member, IEEE) received the B.Sc. degree in computer science from the University of Applied Science Brugg-Windisch, Windisch, Switzerland, in 1997, the PGDip in geographic information systems and the M.Phil(Sc) degree in Earth science from Massey University, Palmerston North, New Zealand, in 2005 and 2006, respectively, and the Ph.D. degree in geography from the University of Zurich, Zurich, Switzerland, in 2011.

He was with the APEX project since 2007 and is currently an Academic Associate with the Remote Sensing Laboratories, University of Zurich, responsible for APEX sensor and data calibration and project manager of the forthcoming Airborne Research Facility for the Earth System. His research interests include the calibration of spectrometers and the design of combined database and software systems such as the spectral database SPECCHIO.

**Michael E. Schaepman** (Senior Member, IEEE) received the M.Sc. and Ph.D. degrees in geography from the University of Zurich (UZH), Zurich, Switzerland, in 1993 and 1998, respectively.

In 1999, he was a Postdoctoral Researcher with the Optical Sciences Center, University of Arizona, Tucson, AZ, USA. In 2000, he was appointed as a Project Manager of the European Space Agency APEX spectrometer. In 2003, he became the Full Chair of Geoinformation Science and Remote Sensing with the Wageningen University, Wageningen, The Netherlands. In 2009, he was appointed as the Full Chair of Remote Sensing with UZH, where he headed the Remote Sensing Laboratories, Department of Geography. In 2020, he became the President of UZH. His research interests include computational Earth sciences using remote sensing and physical models, with a particular focus on using imaging spectroscopy for biodiversity mapping.

**Mathias Kneubühler** received the M.S. degree in geography and the Ph.D. degree (Dr. sc. nat.) in remote sensing, with emphasis on spectral assessment of crop phenology, from the University of Zurich, Zurich, Switzerland, in 1996 and 2002, respectively.

He is currently leading the Spectroscopy Group, Remote Sensing Laboratories, University of Zurich. His research interests include spectrodirectional data analysis and spectral assessment of phenological processes in vegetated ecosystems.